Journal of Manufacturing Processes 135 (2025) 253–268

Contents lists available at ScienceDirect

Journal of Manufacturing Processes

journal homepage: www.elsevier.com/locate/manpro

Unravelling the influence of CMT characteristic parameters on process stability and joint properties in dissimilar aluminium-steel weld-brazing

Jaivindra Singh [a,*], Kanwer Singh Arora [b], J.P. Oliveira [a]

[a] CENIMAT/i3N, Department of Materials Science, NOVA School of Science and Technology, Universidade NOVA de Lisboa, Caparica 2829-516, Portugal
[b] Research & Development, Tata Steel Limited Jamshedpur, Jharkhand 831001, India

ARTICLE INFO

Keywords:
Steel
Aluminium
Weld-brazing
Process stability
Wettability
Microstructure
Shear-tensile strength

ABSTRACT

This study evaluates the stability and performance of Cold Metal Transfer (CMT) weld-brazed joints by examining the effects of boost current, boost duration, wait current, and wire feed rate (WFR) during the wait phase. Process stability improves on increasing boost current, while longer boost durations (>4 ms) or higher wait currents (>80 A) can cause instability due to arc disturbances and premature filler deposition. The WFR influences the deposition frequency but does not significantly impact stability. Wettability improves with increased boost current, boost duration, and wait current. However, excessive wettability can cause processing-induced defects such as solidification cracking due to both reduced cross-sectional area and presence of highly brittle intermetallic layer. The thickness of the intermetallic layer grows with increasing heat input. Shear-tensile tests revealed that the failure load rises with boost current, duration, and wait current up to an optimal level, then declines primarily due to excessive intermetallic layer thickness (>5 μm). The failure modes varied with layer thickness and wettability, with the highest load observed at a WFR of 10 m/min.

1. Introduction

Lightweighting of vehicle structures has become a primary priority for automobile manufacturers to enhance fuel efficiency and reduce environmentally hazardous emissions [1,2]. The use of a combination of thin zinc-coated high-strength steels and aluminium alloys in automobile production ensures both crash resistance and lightweight design [3,4]. Therefore, joining dissimilar or multi-materials has become an essential yet challenging task, particularly in achieving a mechanically sound joint [5]. In case of aluminium-steel joining, this challenge arises from the significant differences in the thermo-physical properties (such as melting point, thermal conductivity and coefficient of thermal expansion) and the low miscibility of these materials resulting in their poor metallurgical compatibility [6,7]. During dissimilar joining of aluminium to steel, welding occurs between the molten aluminium-based filler and the aluminium base plate, while brazing takes place between the steel and the molten filler. This combination of processes is referred to as weld-brazing [8]. This trend toward lightweight design presents significant technical challenges, particularly when it comes to achieving reliable and durable joints between materials with vastly different thermophysical properties, such as aluminium and steel.

Due to the nearly zero mutual solid solubility between iron (Fe) and aluminium (Al), a hard and brittle intermetallic layer composed of Fe—Al compounds forms at the interface aluminium and steel [9,10]. Research has shown that the thickness of this intermetallic layer increases with heat input [11,12]. As the thickness of the intermetallic layer grows, the brittleness of the interfacial area in dissimilar joints also increases, making them more prone to failure [13]. Several researchers have attempted to improve the mechanical integrity of aluminium-steel joints using various methodologies, including: (i) modifications in filler composition [14], (ii) optimization or adjustment of process parameters [15], (iii) use of interlayers [16,17], (iv) modifications in the joining process [18], and (v) surface treatments and coatings [19]. It can be concluded from the literature that the use of aluminium-based silicon (Si) enriched fillers can significantly reduce the thickness and brittleness of the interfacial layer. This results in the formation of ternary Fe-Al-Si intermetallic phases instead of hard and brittle Fe—Al binary intermetallics, thereby significantly improving joint strength [20,21]. However, in dissimilar steel-aluminium joining, the formation of intermetallic phases is unavoidable, often rendering the interface the weakest, most failure-prone site in the joint [1,22]. This ongoing challenge highlights the need for further innovation in joining techniques to

* Corresponding author.
E-mail address: j.singh@fct.unl.pt (J. Singh).

https://doi.org/10.1016/j.jmapro.2025.01.040
Received 14 September 2024; Received in revised form 18 January 2025; Accepted 19 January 2025
Available online 22 January 2025

Table 1
Chemical composition of base materials and filler wire (in wt%).

DP 780	C	Si	Mn	Cr	Al	Cu	Fe	Others
	0.16	0.25	1.8	0.4	0.04	0.04	Bal.	
AA5052	Si	Fe	Cu	Mn	Mg	Cr	Ti	Al
	0–0.25	0–0.4	0–0.1	0–0.1	2.2–2.8	0.1–0.35	0–0.05	Bal.
AlSi5	Si	Fe	Cu	Mn	Mg	Zn	Ti	Al
	4.5–6	<0.8	<0.3	<0.05	<0.05	<0.1	<0.20	Bal.

minimize the detrimental effects of intermetallic phase formation and enhance the long-term performance of steel-aluminium joints.

The wettability of the deposited filler on the steel plays a crucial role in determining the mechanical properties of lap weld-brazed joints, as it is a measure of the contact area between the filler and the steel. The wettability is greatly influenced by the heat input as well as the composition of filler wire. Milani et al. [23] reported that the addition of silicon to Al-based fillers not only suppressed the formation of intermetallics at the interface but also improved the fluidity i.e. wettability of filler in molten state. In addition, the wettability of the deposited filler improves with increased heat input [18,24]. Increasing the heat input enhances the melting and spreading of molten filler on the steel surface, leading to greater wetting and an extended contact length between deposited filler and steel [18]. The relationship between the intermetallic layer thickness, wettability, and heat input is highly complex, and their combined effect on the mechanical properties of the joint requires further investigation. A better understanding of how excessive wettability and brittleness in the interfacial region affect the mechanical strength of dissimilar steel-to-aluminium joints is needed. In conclusion, further research is essential to unravel the intricate interactions between wettability, intermetallic formation, and heat input to optimize the performance and durability of dissimilar steel-to-aluminium joints in welding and brazing applications.

Cold Metal Transfer (CMT) process is an emerging welding technique in the automotive sector, valued for its unique and superior characteristics [25]. These include spatter-free, smooth deposition without the pinching phenomenon, low heat input, the ability to efficiently join thin, coated, and dissimilar materials with minimal distortion [26–28]. The working principle of the CMT process is similar to that of metal inert gas (MIG) welding, with the key difference being in deposition: in MIG, deposition occurs due to electromagnetic forces (EMF), while in CMT, deposition is driven by the backward motion of the filler wire [29]. The CMT weld cycle consists of three main phases: the boost phase, wait phase, and short-circuiting phase [15,30]. In the boost phase, the arc initiates melting, forming a droplet at the wire tip [31]. During the wait phase, the droplet grows until it contacts the base metal, enabling smooth deposition via the backward filler motion in the short-circuiting phase [18,32]. Integrating wire motion into process control makes the CMT process unique, as molten filler is deposited through the filler's backward motion at the end of the short-circuiting phase. Key parameters like boost current, boost duration, wait current, and short-circuiting current significantly influence deposition behaviour, microstructure, and mechanical properties of the weld joints [33,34]. Chen et al. [35] reported that adjusting CMT parameters influences droplet size, penetration depth, and bead width during bead-on-plate CMT welding of 3 mm thick Q235 mild steel. They observed a significant increase in weld width with an increase in boost current and boost duration, though the reinforcement did not vary significantly. However, this area remains unexplored for the dissimilar joining of aluminium to steel. Further research is necessary to explore the

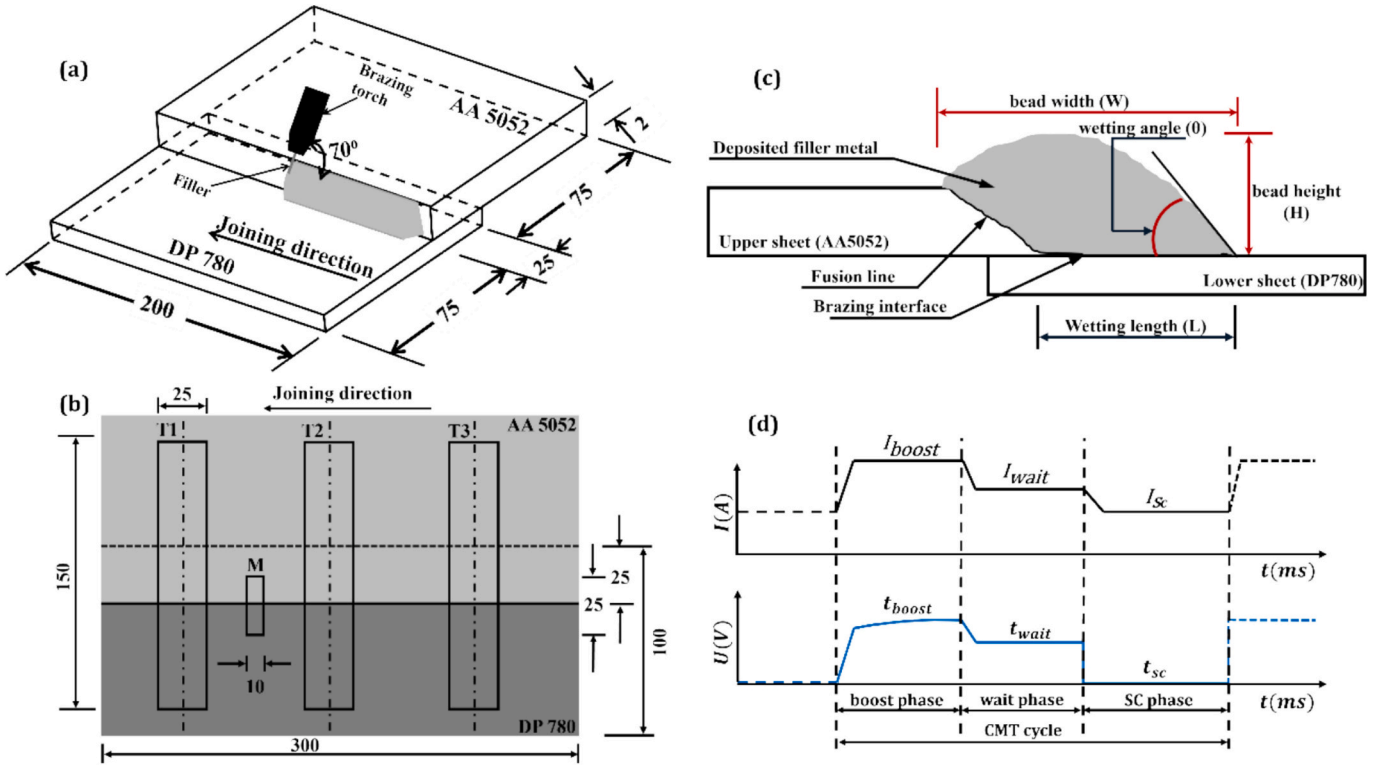

Fig. 1. Schematic representation of (a) the experimental setup, (b) the cross-section of the weld-brazed joint, (c) the variation in voltage and current during the CMT process, and (d) location and dimensions of tensile (T1, T2 & T3) and metallography (M) specimens (all units are in mm).

Table 2
Different weld-brazing parameters used in this work.

S. no.	I_{boost} (A)	t_{boost} (ms)	I_{wait} (A)	Vd_{wait} (m/min)	Heat input (J/mm)
S1	150	2	60	20	103
S2	160	2	60	20	124
S3	170	2	60	20	131
S4	180	2	60	20	136
S5	200	2	60	20	141
S6	220	2	60	20	150
S7	150	4	60	20	160
S8	150	6	60	20	183
S9	150	8	60	20	193
S10	150	12	60	20	204
S11	150	2	80	20	150
S12	150	2	100	20	174
S13	150	2	120	20	211
S14	150	2	60	15	124
S15	150	2	60	10	120
S16	150	2	60	5	117

influence of CMT characteristic parameters on the quality and performance of dissimilar steel-to-aluminium welds, as the unique challenges posed by this material combination require a deeper understanding of how these parameters affect joint properties and weld integrity.

The bottleneck in dissimilar joining technologies is the control and suppression of hard and brittle Fe—Al intermetallic formation at the interface. This study addresses critical challenges in dissimilar steel-aluminium joining, particularly the control of brittle Fe—Al intermetallic formation at the interface. By investigating the influence of various CMT characteristic parameters on process stability, microstructure, and mechanical properties, this work fills key research gaps. The evaluation of process stability through cyclograms and probability distribution curves provides valuable insights. These findings contribute to a deeper understanding of CMT process, offering potential to optimize parameters for enhanced joint integrity and durability in automotive applications.

2. Experimental procedures

In the present work, dissimilar joining of aluminium alloy (AA5052) of 2 mm thickness and 1.2 mm thick zinc coated dual phase steel (DP780) was performed in lap configuration (25 mm overlapping) using Al based Si enriched (AlSi5) filler wire of 1.2 mm diameter. DP780 steel was galvanized coated (coating layer was composed of almost pure Zn) with a coating thickness of about 10–15 μm on both sides. The thicker aluminium sheet enables faster heat dissipation from the joint area and enhances the overall load-bearing capacity of the joint. In contrast, the 1.2 mm thick high-strength steel sheet contributes to a lightweight design without compromising strength. The chemical composition of

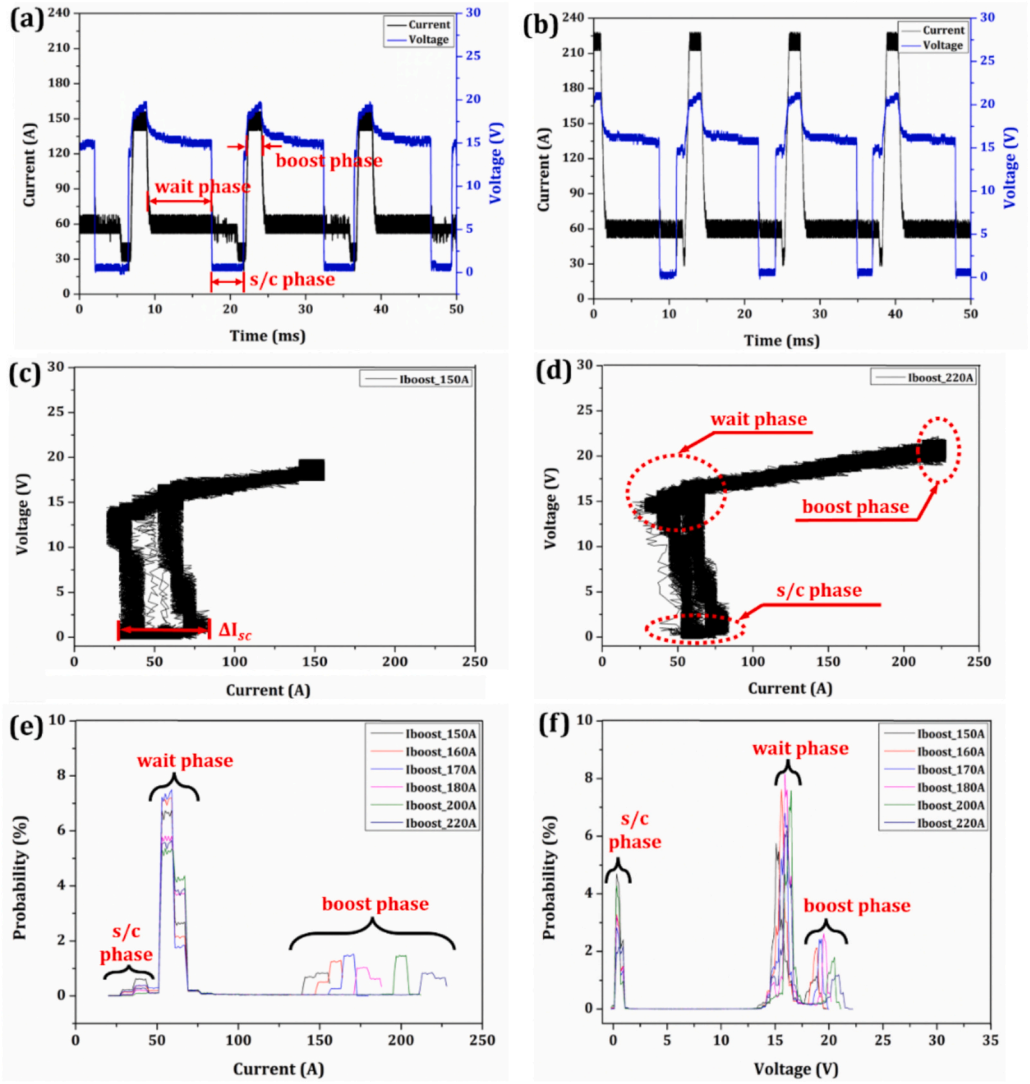

Fig. 2. Effect of varying boost current levels on (a, b) voltage-current waveforms, (c, d), cyclograms, and (e, f), probability distribution curves.

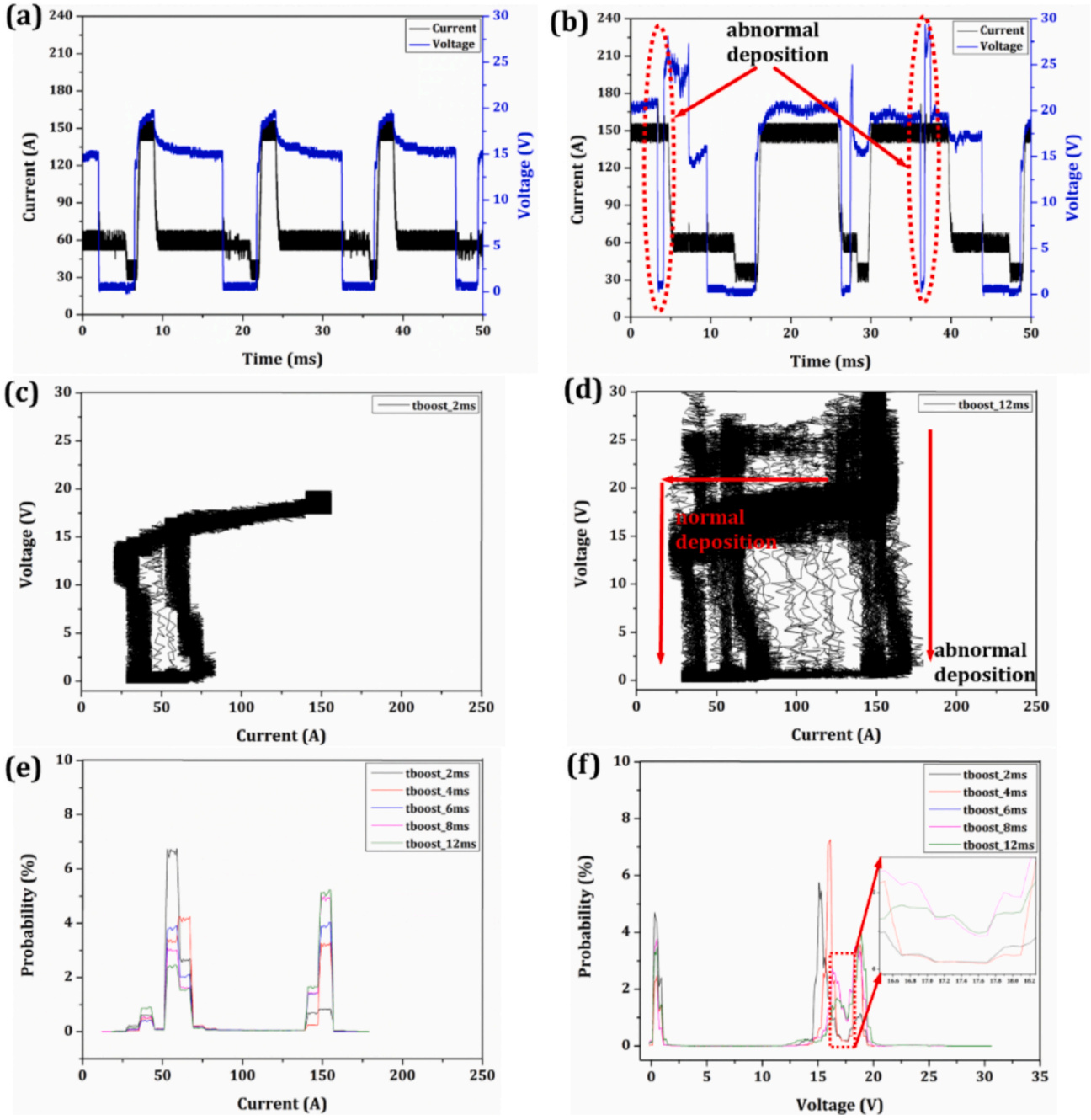

Fig. 3. Effect of varying boost duration levels on (a, b) voltage-current waveforms, (c, d), cyclograms, and (e, f), probability distribution curves.

both base metal sheets and filler wire is given in Table 1. Surfaces of the sheets were cleaned using acetone prior to the joining to remove dirt and other impurities, and then brazed with the rolling direction of both sheets parallel to the joining direction. Pure argon (99.99 %) was used as shielding gas at a flow rate of 12 lpm to protect the molten pool from atmospheric contaminations. Fig. 1(a) describes the schematic of joining procedure.

The manufacturer provides several synergic lines, each programmed for different processes and filler materials, which can be utilized by selecting the appropriate filler diameter and WFR. These synergic lines feature fixed values for various characteristic parameters intended to produce sound weld joints. In this study, the characteristic parameters were adjusted using a remote-control unit (RCU) integrated with a CMT power source. The different sets of characteristic parameters are listed in Table 2. Sample 1 corresponds to the synergic line programmed for the CMT process with a 1.2 mm diameter AlSi5 filler and 4 m/min WFR. Samples 2 through 16 exhibit variations in parameter levels, including boost current, boost duration, wait current, and WFR during the wait phase. The terms boost current, boost duration, and wait current are also commonly known as arc current, arc duration, and background current, respectively. The speed was kept constant at 400 mm/min for all the experiments. In this work, the WFR during the wait phase was changed directly from the machine control unit without measuring the real-time variation of the WFR during all other phases. Although the overall WFR was kept constant at 4 m/min for all experiments, there is a possibility that the overall WFR might have changed slightly when the WFR during the wait phase was altered. Heat input was calculated using Eq. (1) [36].

$$HI = \eta \frac{\sum U_i I_i}{V} \quad (1)$$

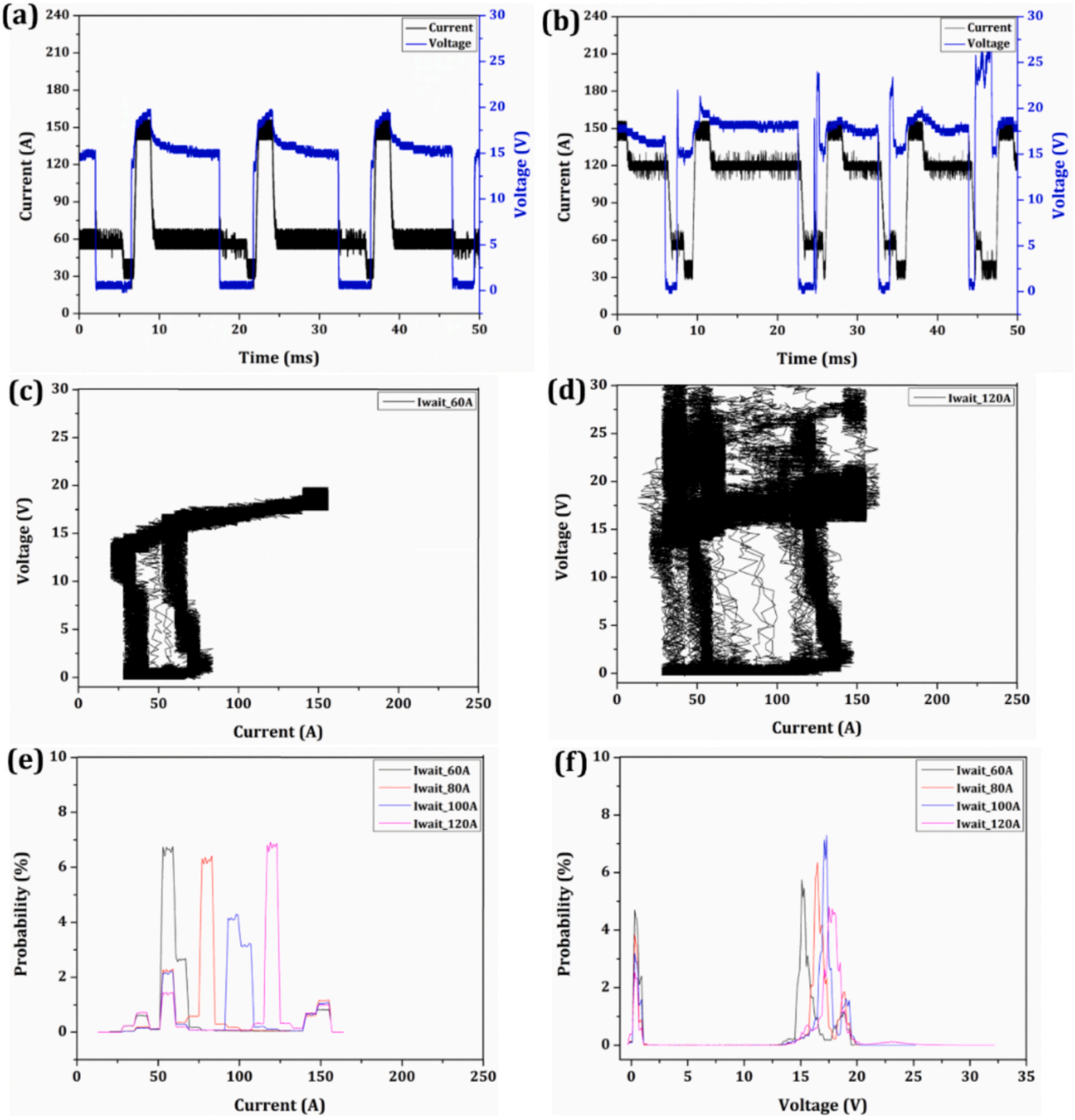

Fig. 4. Effect of varying wait current levels on (a, b) voltage-current waveforms, (c, d), cyclograms, and (e, f), probability distribution curves.

where V is the brazing speed, η (~0.85) is thermal efficiency of CMT process [37], and U_i and I_i represent the instantaneous voltage and instantaneous current, respectively.

Samples for metallography and shear-tensile testing were machined in the transverse direction relative to the brazing as shown in Fig. 1(b). During tensile testing, three samples were tested for each parametric condition to minimize variability in failure load measurements and to obtain an average value. Shear-tensile testing was performed at a crosshead speed of 1 mm/min. The metallography samples were polished using abrasive papers and diamond slurries to a 0.25 μm finish and subsequently etched with Kroll's etchant. Subsequently, these samples were examined under optical microscope (OM) and scanning electron microscope (SEM) equipped with energy dispersive X-ray spectroscopy (EDS). A schematic of the cross-section of the weld-brazed joint is shown in Fig. 1(c). The joints were characterized using various bead parameters, including bead width, wetting length, wetting angle, and fusion area. Voltage-current (V—I) transients were recorded with oscilloscopes for all experiments. Fig. 1(d) shows the schematic of the voltage and current waveforms during the CMT process.

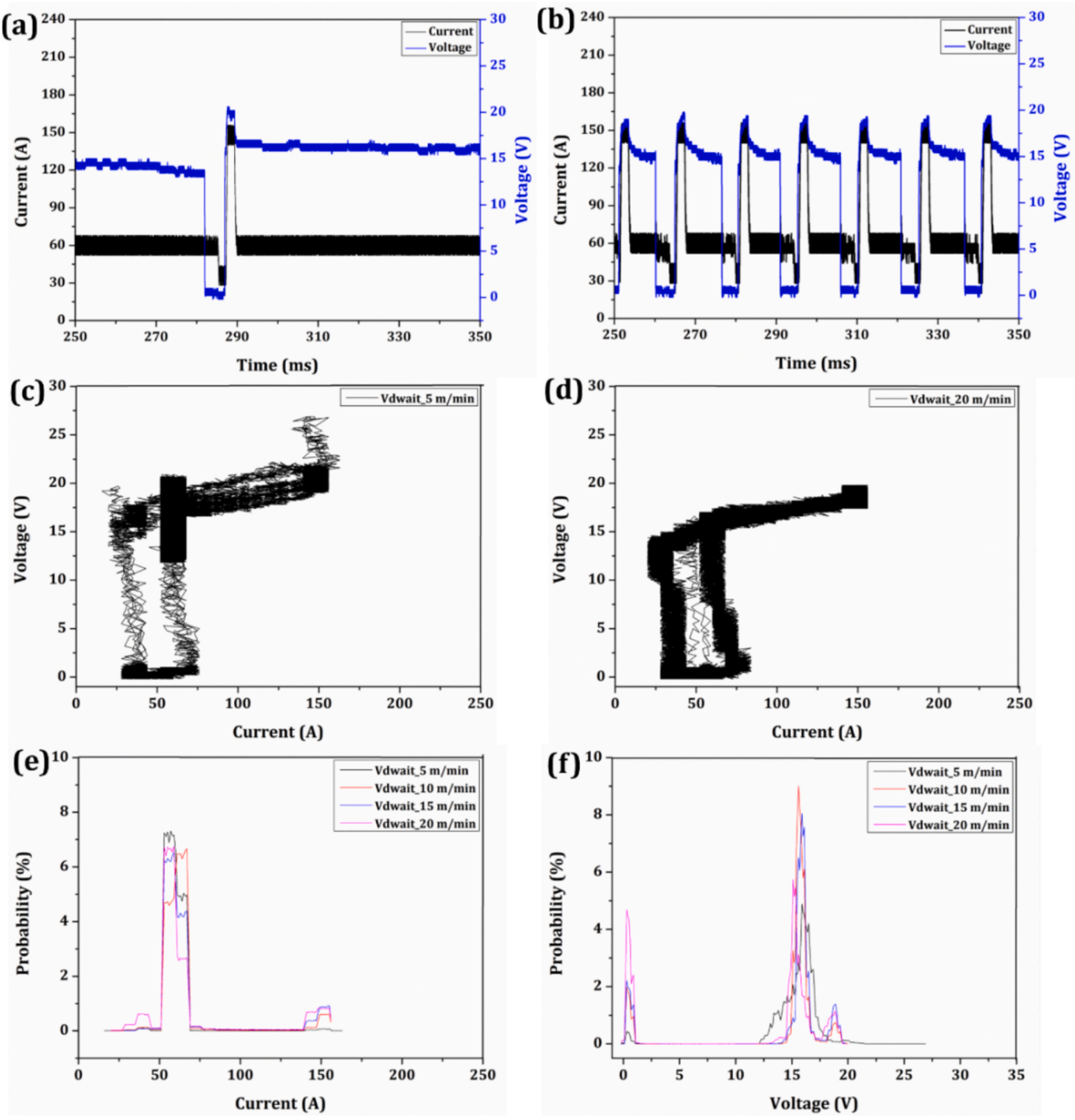

Fig. 5. Effect of varying WFR during wait phase on (a, b) voltage-current waveforms, (c, d), cyclograms, and (e, f), probability distribution curves.

3. Results and discussion

3.1. Process stability

The stability of a welding process depends on several factors, including welding speed and mode of operation, shielding gas composition, surface conditions of the workpiece, welding current and arc voltage, for example. V—I variation, cyclograms, and probability distribution curves are essential tools for assessing the stability of welding processes. V—I transients capture real-time fluctuations in arc current and voltage, highlighting instability events like irregular arc behaviour. Cyclograms, by plotting voltage against current in a cyclic manner, reveal the dynamic relationship between these parameters and show how stable operational points repeat over time [38,39]. Probability distribution curves convert V—I data into a statistical framework, showcasing repeatability by analysing the spread and concentration of values. To plot the probability distribution curves, the recorded time-domain data for voltage and current was converted to the probability domain using appropriate filters. These curves are directly influenced by CMT characteristic parameters. The integration of these three methods provides a holistic view of process stability, enabling innovative optimization of CMT parameters for more reliable and efficient welding operations. In the present work, V—I transients, cyclograms, and probability distribution curves were plotted to determine the stability of the

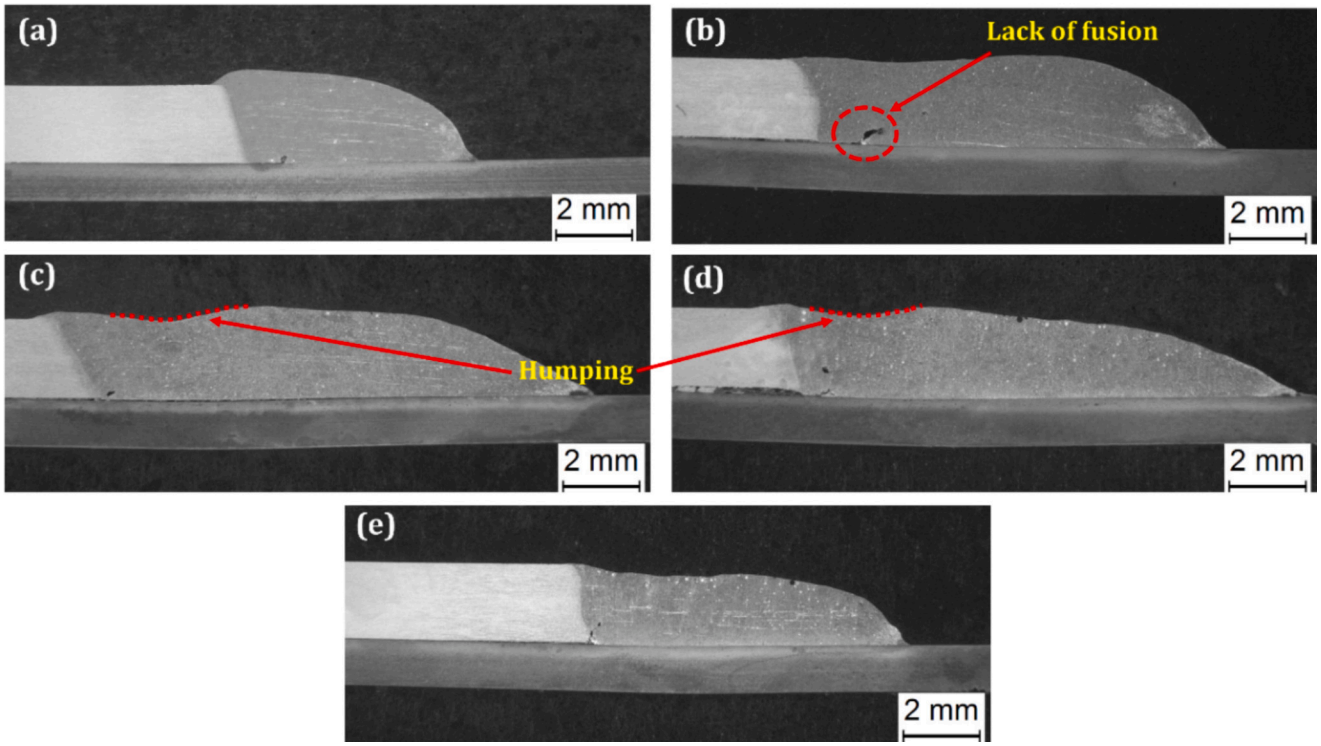

Fig. 6. Cross-sections of various weld-brazed joints as listed in Table 2: (a) S1, (b) S6, (c) S10, (d) S13, and (e) S16.

CMT weld-brazing process at different CMT characteristic parameters, including boost current, boost duration, wait current, and WFR during the wait phase. It should be noted that in a CMT weld cycle, the terms boost current, boost duration, and wait current are also commonly referred to as arc current, arc duration, and background current, respectively [40,41].

Fig. 2 depicts the variation of V—I transients, cyclograms, and probability curves with an increase in the boost current from 150 to 220 A. An increase in boost current leads to an increase in arcing power, which in turn increases the heat input of the process [42]. The V—I curves are relatively smooth and have no abnormal peaks, indicating that the CMT process remains stable despite the increase in boost current (Fig. 2(a & b)). The cyclogram of the CMT process appears as the Greek letter gamma (Γ) (Fig. 2(c & d)). The width of the vertical leg represents the variation in short-circuiting current during the deposition of molten filler, while the length of the horizontal leg represents the level of boost current [18]. In the present work, the length of the horizontal leg increased with the boost current. The cyclogram becomes denser (narrow vertical leg) when the boost current is increased from 150 A to 220 A, signifying that the stability of the CMT process is even better at higher boost current levels. In the current probability curve (Fig. 2(e)), the distinct peaks of boost current can be seen depending on its value, whereas the peaks of all three phases overlap in the voltage probability curve (Fig. 2(f)), indicating that the process remains stable, and the deposition is smooth as the boost current increases.

The arcing power can be increased either by raising the boost current or by extending the boost duration [42]. Fig. 3 shows the variation of V—I transients, cyclograms, and probability curves as the boost duration is increased from 2 to 12 ms. It can be seen that there are some abnormal peaks and valleys in the middle of the boost phase voltage when the duration is increased to 12 ms (Fig. 3(a & b)). These abnormalities in the voltage curve can be attributed to disturbances in the arc and the corresponding deposition of the molten droplet. A too-long boost period leads to the availability of surplus energy to melt the filler wire, causing premature deposition of a fraction of molten filler droplets in the absence of a wait phase. Ideally, the molten droplet grows during the wait phase until it contacts the base metal surface. However, with a high boost duration, the excessive arc power causes disturbances in both the arc and the deposition process. The cyclogram at 2 ms boost duration has the ideal gamma (Γ) shape, clearly showing all three phases (Fig. 3(c)). In contrast, increasing the boost duration results in a very complex shape of cyclogram. At higher boost duration the shape of cyclogram is nearly rectangular and an increase in the width of the vertical leg indicates unstable deposition of the molten filler (Fig. 3(d)). The denser part on the right side of the vertical leg of cyclogram at a 12 ms boost duration shows deposition in the absence of wait phase i.e. abnormal/premature deposition. In this abnormal/premature deposition, the voltage suddenly drops from the boost phase value to the short-circuiting value, as also evident in the voltage waveform (Fig. 3(b)). In normal CMT deposition, the wait phase occurs during the transition from the boost phase to the short-circuiting phase as shown in Fig. 2(a). The current probability curve (Fig. 3(e)) is relatively normal and shows no abnormalities, which is attributed to the controlled and smooth variation of current on increasing boost current as all three phases can be distinguished in the current waveform. However, some unusual variations are observed in the voltage probability curves (Fig. 3(f)). The transition between the wait phase and the boost phase indicates higher possibility of arc disturbance as evident from higher probability values in this region, especially at longer boost durations (8 and 12 ms) compared to shorter boost durations. This observation clearly suggests that the CMT process becomes unstable at higher boost duration values. Therefore, it is recommended to keep the boost duration at lower levels, such as 2 or 4 ms. Another possible approach to increase arcing power is to simultaneously increase the boost current and boost duration, which requires further investigation [30].

Since the wait phase is also a part of the arcing phase, the wait current was increased to increase the arcing power [43]. Fig. 4 depicts the V—I transients, cyclograms, and probability curves with the wait current increased from 60 to 120 A. The comparatively higher noise in the current signal and the abnormal peaks and valleys in the voltage waveform clearly indicate that the CMT process was less stable at higher wait phase current values (Fig. 4(a&b)). These variations in the voltage

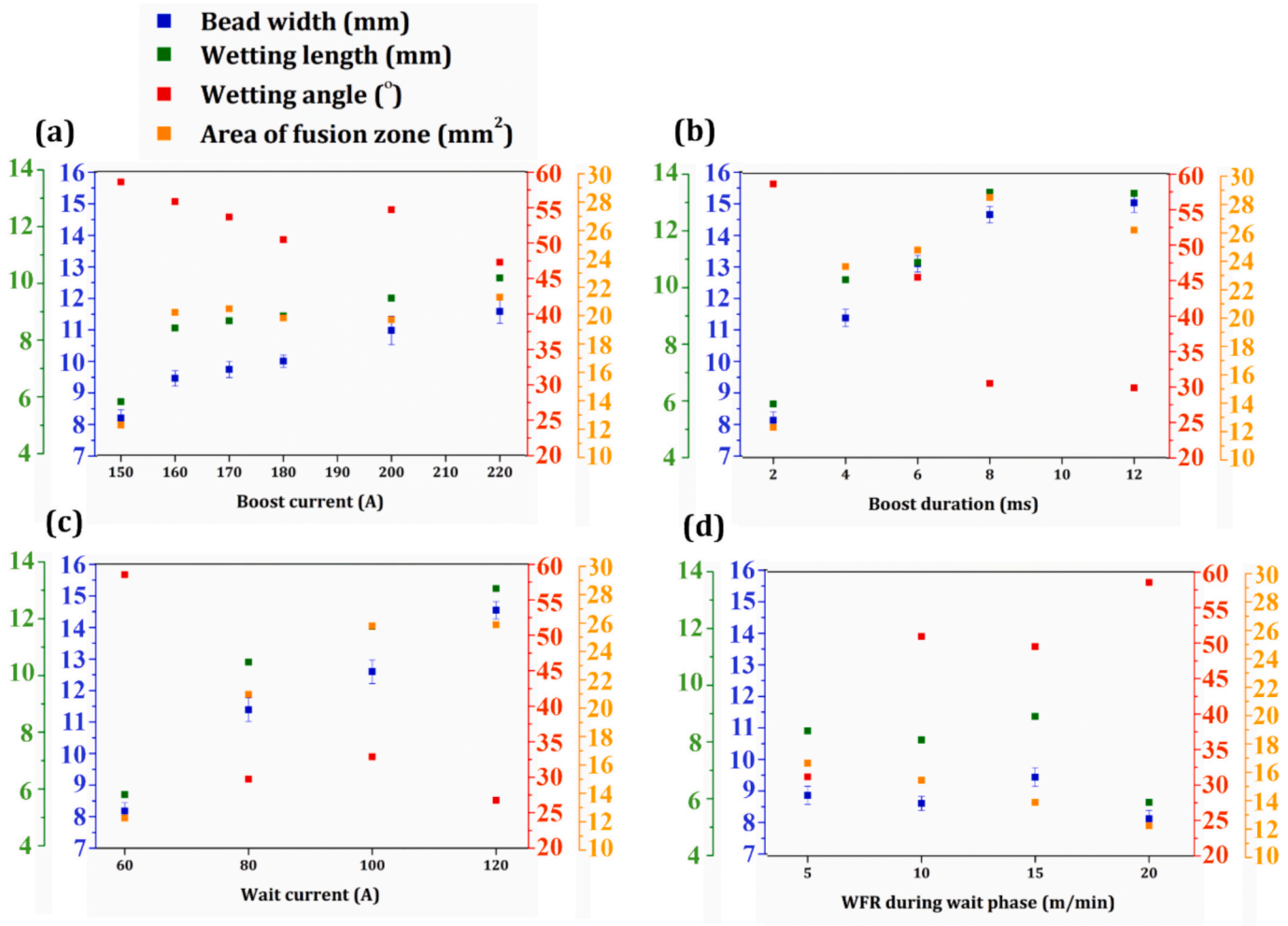

Fig. 7. Variation of bead parameters with CMT characteristic parameters: (a) boost current, (b) boost duration, (c) wait current, and (d) WFR during the wait phase.

curve at 120 A wait current are very similar to those observed at higher boost durations. Additionally, the cyclogram transformed into a rectangular shape at higher wait phase current, similar to the case of higher boost durations, which describes occurrences of premature/abnormal deposition in the absence of the wait phase and the corresponding arc disturbances (Fig. 4(c & d)). The current probability curve clearly shows distinct peaks of wait phase current depending on its level, with no indication of variation in stability (Fig. 4(e)). However, the voltage probability curve clearly shows signs of poor stability at 120 A, as there was a common peak for the wait and boost phases (Fig. 4(f)). This can be attributed to the nearly horizontal/constant voltage line during the boost-wait phase, which otherwise gradually declines during the wait phase at lower wait current levels.

Another parameter included in this study is the feed rate of the filler wire during the wait phase. The wait phase is known for the growth of the molten droplet at the tip of the filler wire until it reaches a sufficient size or volume to contact the base metal surface and deposit [15,18]. Increasing the feed rate of the filler during the wait phase reduces the time for droplet deposition, i.e., the duration of the wait phase, by melting the increased volume of filler more quickly and thus increasing the droplet size rapidly [43]. This is how the frequency of droplet deposition increases with the WFR. The increase in deposition frequency can be confirmed by examining the short-circuiting frequency (V—I transients in the Fig. 5(a & b)). It can be seen that short-circuiting occurs only once in a period of 100 ms at 5 m/min WFR, whereas it occurs six times in the same period at 20 m/min WFR. Thus, it can be deduced that WFR during wait phase controls the duration of wait phase which in turn influences the deposition frequency. The cyclogram appears normal at both levels of WFR, indicating that process stability is not significantly affected by WFR during this phase (Fig. 5(c & d)). The cyclogram at 5 m/min is less dense compared to the one at 20 m/min, which can be attributed to the lower number of CMT cycles at 5 m/min compared to 20 m/min WFR. The probability curves for voltage and current are smooth, and all three peaks of different CMT phases are clearly visible (Fig. 5(e & f)). One interesting observation from the voltage probability curve at 5 m/min WFR is that it has a high peak for the wait phase, whereas it has a very small peak for the short-circuiting phase and nearly a flat line for the boost phase. This indicates that most of the time was spent in the wait phase, as the 5 m/min WFR during the wait phase was too low for faster growth and deposition of the filler metal.

3.2. Joint geometry

Bead shape/geometry play an important role in the evolution of the mechanical properties of weld-brazed lap joints. Fig. 6 shows the bead geometry of joints weld-brazed using different CMT characteristic parameters. The bead of the base parametric set (S1) is narrow and bumpy compared to all other joints (Fig. 6(a)). This difference can be attributed to the increase in heat input when the boost current, boost duration, and wait current are increased independently (refer to Table 2). In addition, there is a noticeable hump in joints weld-brazed at the maximum levels of boost duration and wait current due to strong arc forces (Fig. 6(c & d)). In addition, a discontinuity/defect is present at the root of all the weld-brazed joints (Fig. 6(b)). This defect, also known as lack of fusion,

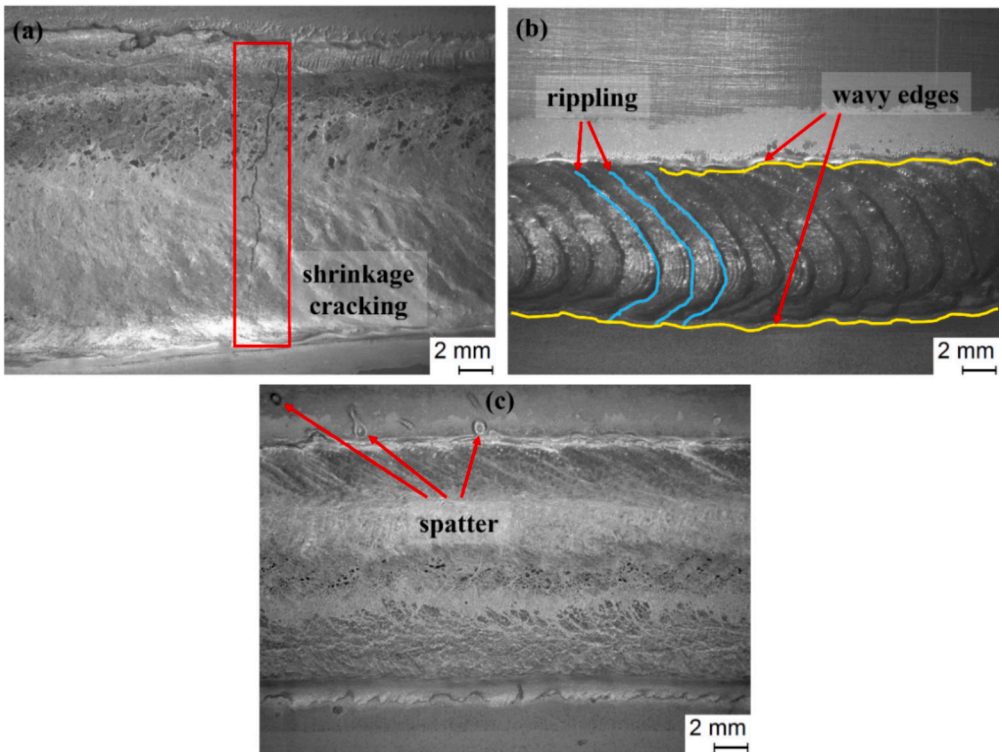

Fig. 8. Defects in weld-brazed joints observed in different samples listed in Table 2: (a) S13, (b) S16, and (c) S10.

forms due to the influence of zinc-rich fumes. When the molten filler is deposited onto the coated steel surface, it melts and partially evaporates the zinc coating. Molten zinc accumulates at the corners of the deposited bead, and zinc fumes attempt to escape from the joint area through the gap between the sheets being brazed. This further leads to the formation of the discontinuity at the root upon solidification. Singh et al. [8] systematically characterized this zone at the root of weld-brazed joints, identifying it as composed of zinc-rich phases. They also proposed introducing a predefined gap between the sheets to allow zinc fumes to escape more easily from the joint area and achieved a significant reduction in the area of this zinc rich zone at root using 0.1 and 0.2 mm predefined gap between the sheets. However, this gap can cause additional bending during shear-tensile testing of lap weld-brazed joints, leading to joint failure at lower loads. In the present work, the bead geometry was characterized using various parameters, namely bead width, wetting length, wetting angle, and area of the fusion zone.

Fig. 7 details the variation of different bead parameters with various CMT characteristic parameters. An increasing trend is observed in the wetting length and bead width with increasing boost current, boost duration, and wait current, which can be attributed to a corresponding rise in heat input (Fig. 7(a-c) & Table *2*). Conversely, the wetting angle decreases as the boost current, boost duration, and wait current increase, due to the same reason. A rise in heat input increases the spreadability of molten filler over the steel surface. Therefore, it can be confirmed that the wettability of weld-brazed dissimilar steel-aluminium joints improves with increasing boost current, boost duration, and wait current, as indicated by the increasing wetting length and decreasing wetting angle. On the other hand, excessive wetting can adversely affect the joint properties. Excessive wettability occurs when the wetting angle is excessively low, leading to an over-spreading of the filler material on the steel surface. This overspreading reduces the effective cross-sectional area of brazed lap joints, which can weaken joint strength and introduce variability in joint properties. While a certain level of wettability is essential for effective bonding, excessive wettability can adversely affect joint integrity by altering the distribution of the filler material. In the present work, shrinkage/solidification cracking was observed in the joints at both high boost duration and high wait current levels (Fig. 8(a)), primarily due to excessive wettability. The excessive spreading of molten filler leads to faster solidification, making the joints prone to shrinkage cracking, especially since the interface is already very hard and brittle in the case of steel-aluminium dissimilar joints.

The fusion zone area exhibits an increasing trend with the three CMT characteristic parameters: boost current, boost duration, and wait current, except for slight deviations observed with rising boost current (Fig. 7(a-c)). As shown in Table 2, the heat input increases independently with each of these three parameters. Consequently, the increase in fusion zone area can be attributed to the greater melting volume of the aluminium plate and its subsequent inclusion in the fusion zone as heat input rises. Conversely, the wettability of the joints decreases with increasing wire feed rate (WFR) during the wait phase, as indicated by the rising wetting angle and reduced wetting length (Fig. 7(d)). This behaviour can be attributed to the higher volume of filler wire being supplied per unit time and length during the wait phase at nearly the same heat input, which diminishes its spreadability when melted and deposited onto the steel surface.

Table 2 shows that the heat input remained relatively consistent, ranging only from 117 to 120 to 124 J/mm as the WFR during the wait phase increased from 5 to 10 to 15 m/min. For this reason, the fusion zone area also decreased with higher WFR during the wait phase, likely due to the reduction in spreadability. Additionally, rippling was observed in the joints at lower WFRs, which is attributed to the longer wait period, i.e., reduced deposition frequency (Fig. 8(b)). Ortega et al. [44] also reported that comparatively larger droplets form at lower WFR values during the wait phase which could also be a possible reason for rippling. Fig. 8(c) shows the spatter caused by disturbances in metal deposition and arc both at larger boost duration and higher wait current values.

3.3. Microstructure

The microstructure of steel-aluminium dissimilar joints is highly

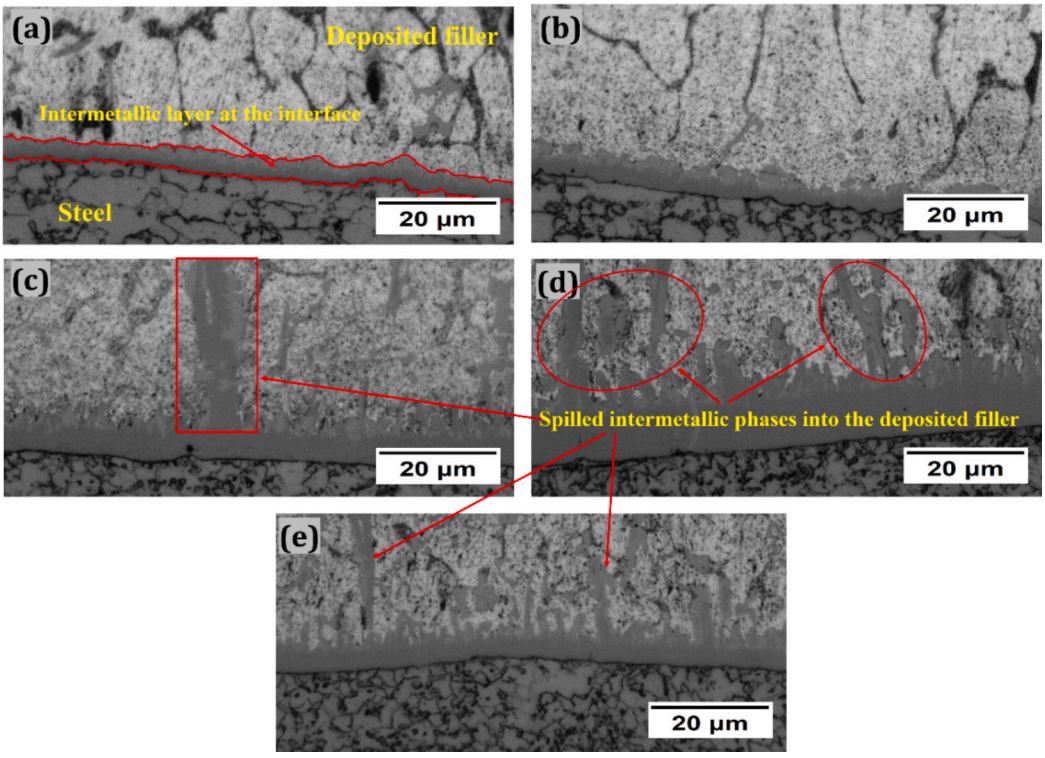

Fig. 9. Micrographs of the intermetallic layer at the interface of various weld-brazed joints, corresponding to the samples listed in Table 2: (a) S1, (b) S6, (c) S10, (d) S13, and (e) S16.

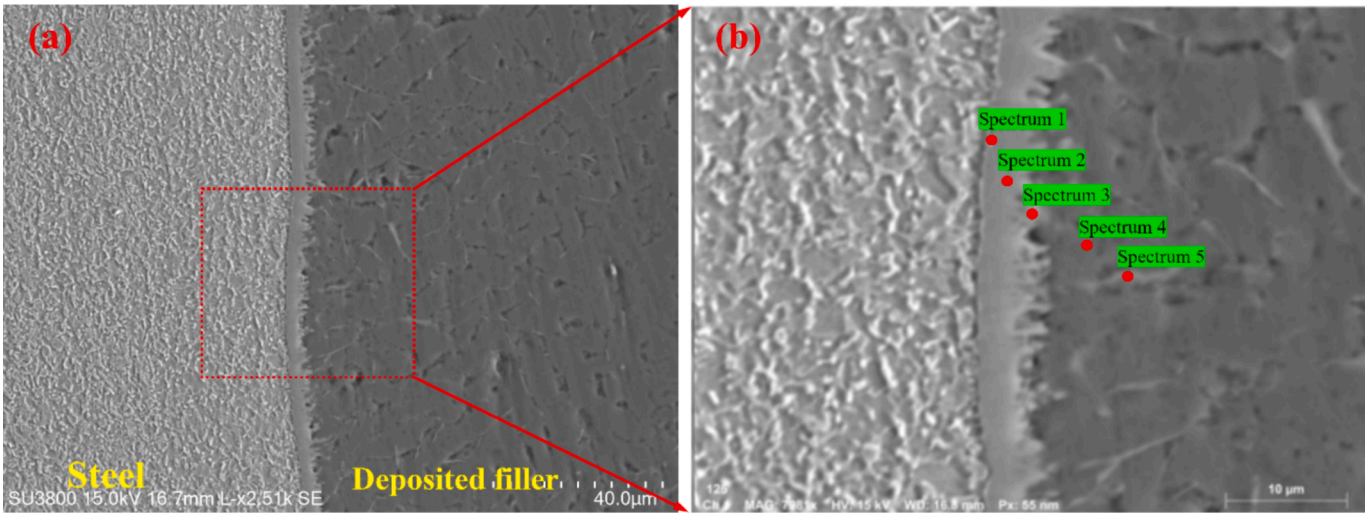

Fig. 10. Location of point EDS analysis at the interface of sample 15.

Table 3
Elemental compositions and possible phases at the indicated spots in Fig. 10 (all results are expressed in weight percent).

Spectrum label	Al	Fe	Si	Mn	Zn	Possible phase
1	82.1	13.6	3.7	0.3	0.3	Al_8Fe_2Si
2	81.7	15.9	1.9	0.4	0.1	$Al_{13}Fe_4$
3	90.6	6.2	2.9	0.3		$(Al,Si)_3Fe$
4	99.1	0.8			0.1	Al solid solution
5	88.7	2.2	8.8		0.3	Al-Si eutectic phase

sensitive to heat input, as the interface between the steel and the fusion zone consists of hard and brittle Fe-Al-Si intermetallic compounds. These intermetallics are known to grow with increased heat input [1,22,45]. In this study, a similar continuous intermetallic layer formed at the interface between the steel and the deposited filler metal. Fig. 9 shows the interfacial microstructure of the weld-brazed joints at different CMT characteristic parameters. In this work, the morphology of intermetallic phases was observed to be needle-shaped and irregular near the deposited AlSi5 filler, while more regular, bulkier phases formed closer to the steel interface. To further characterize these intermetallic phases, EDS point analysis was conducted across the interface of the joint with the highest mechanical strength (S15) (refer to Fig. 10), and the results are summarized in Table 3. The data clearly

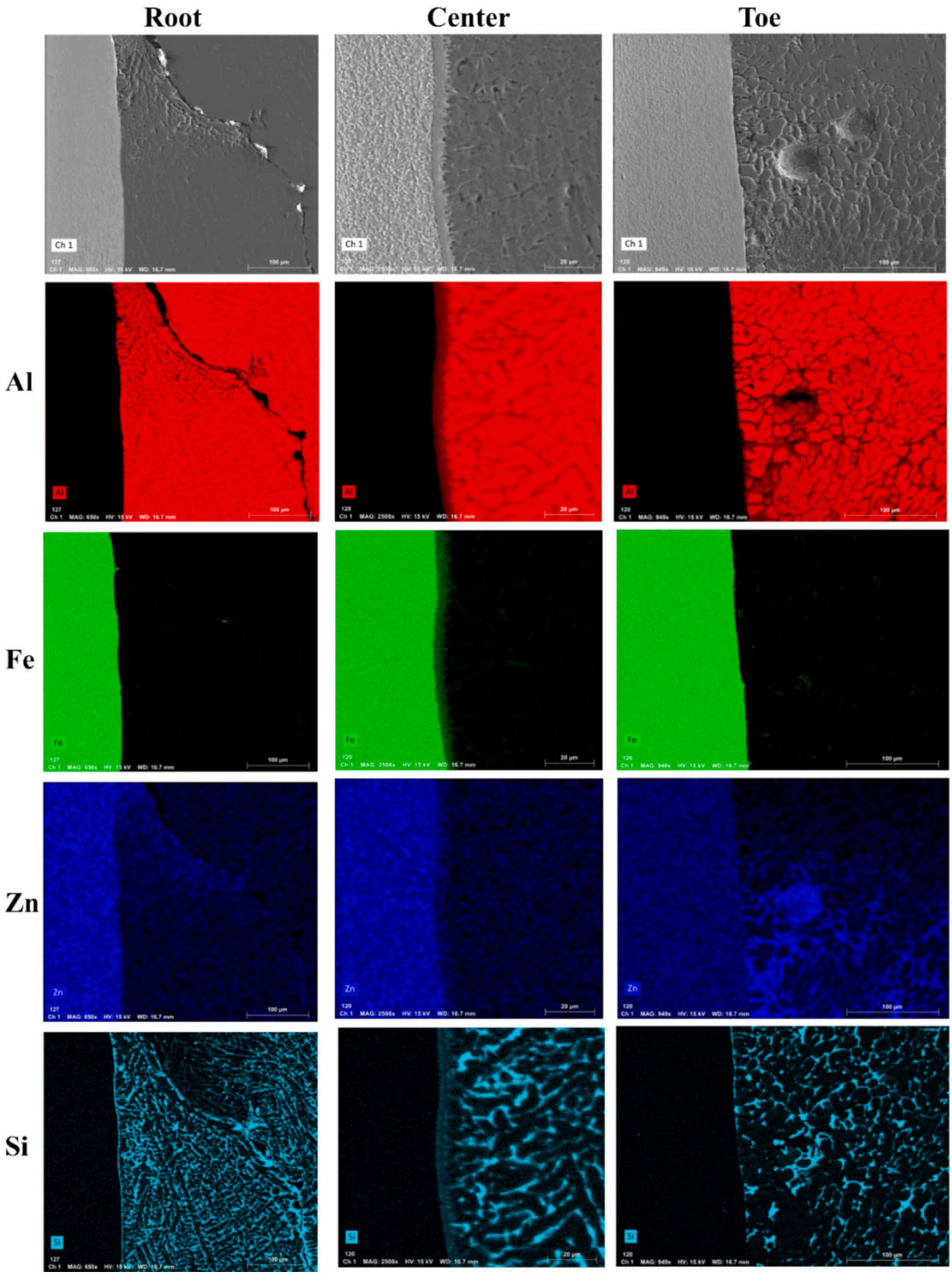

Fig. 11. EDS mapping results for the root, center, and toe regions of sample 15.

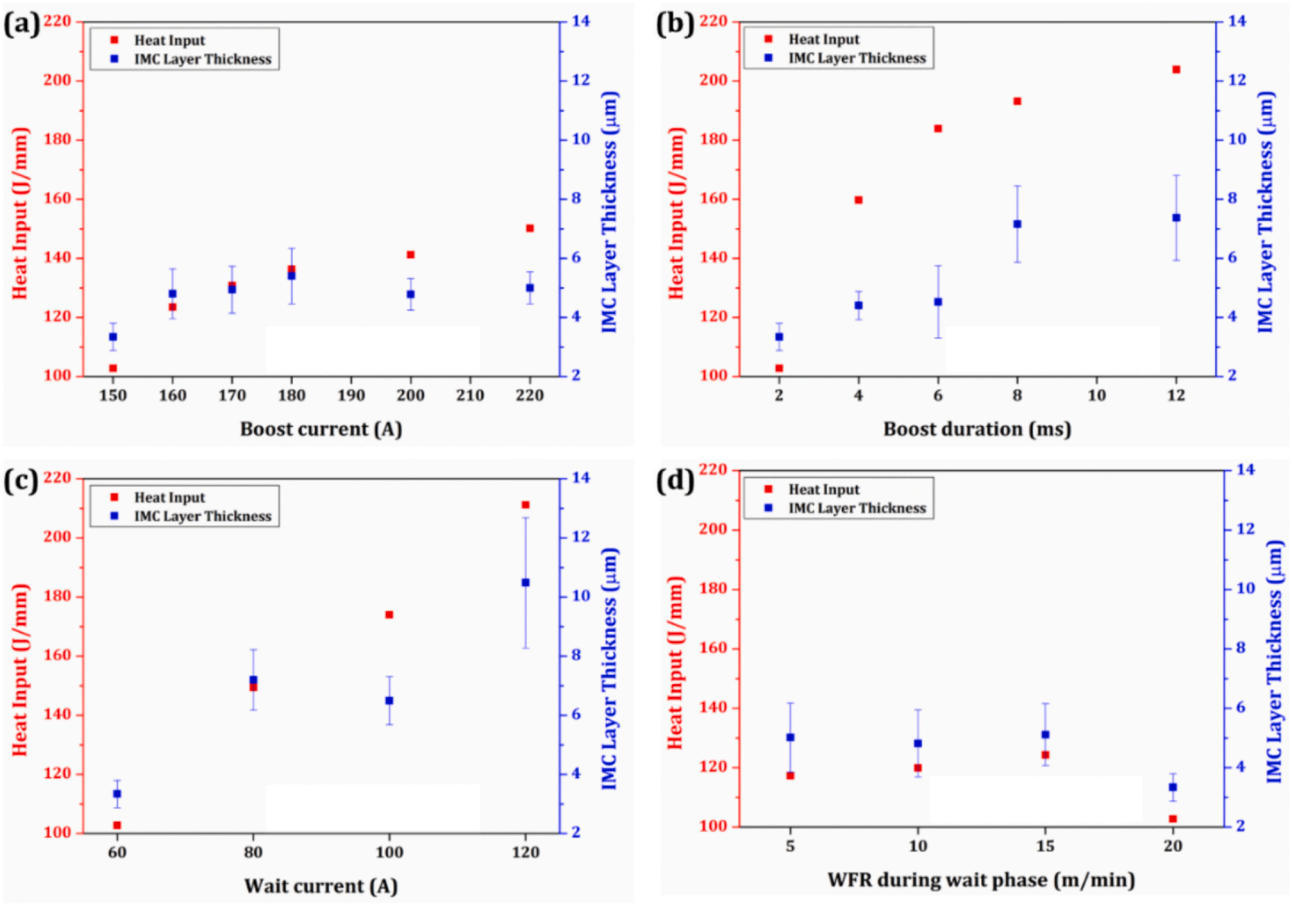

Fig. 12. Variation of heat input and intermetallic layer thickness with different CMT characteristic parameters (a) boost current, (b) boost duration, (c) wait current, and (d) WFR during wait phase.

shows a decrease in Fe across the intermetallic layer when moving toward the deposited filler. Similarly, Si and Al concentrations are highest in the intermetallic layer near the deposited filler and lowest near the steel. This variation in Al, Si, and Fe confirms diffusion across the interface and the formation of Fe-Al-Si ternary intermetallic phases. Based on stoichiometry, the possible intermetallic phases are identified as follows: Al_8Fe_2Si (Spectrum 1) near the steel, as Fe and Si proportions align with this ternary phase; $Al_{13}Fe_4$ (Spectrum 2) in the middle of the intermetallic layer, where Si content is too low for a ternary phase; and $Fe(Al,Si)_3$ near the deposited filler. Consistent with the present work, both Song et al. [21] and Xia et al. [46] reported the formation of two intermetallic phases, two intermetallic phases $Fe(Al,Si)_3$ and $Al_{7.2}Fe_{1.8}Si$, at the interface between steel and the deposited AlSi5 filler during the dissimilar joining of steel to aluminium.

The average thickness of intermetallic compound layer did not change significantly (3.74 ± 0.54 to 4.99 ± 1.35 μm) when the boost current increased from 150 to 220 A (Fig. 9(a & b)). However, excessive growth and spilling of intermetallic phases into the fusion zone were observed at both higher boost duration and higher wait current level (Fig. 9(c & d)), which is attributed to the comparatively higher heat input at these parameters. Further, spilling was also observed at low WFR levels during the wait phase (Fig. 9(e)), but it was less pronounced than in the other two cases. Spilling at low WFR levels can be attributed to the deposition of high-energy, comparatively larger droplets of molten filler into the melt pool, causing turbulence and corresponding spilling into the fusion zone. Fig. 11 shows the EDS area mapping results at the root, center, and toe of the joint which exhibited the highest mechanical strength, aiming to test the hypothesis of Zn accumulation at the corners of the deposited bead under the capillary action. It is evident that no Zn is present at the center of the interface, while Zn accumulation occurs at both the root and toe of the bead. Furthermore, the diffusion of Al, Fe, and Si is more pronounced at the center, whereas it is negligible at the corners. This indicates that the intermetallic layer is thickest at the center, which is exposed to the high-temperature zone of the arc.

To further correlate the growth of intermetallic phases with heat input levels, the intermetallic layer thickness was plotted against heat input for each characteristic parameter, as shown in Fig. 12. While the parameters remained constant, varying a single characteristic parameter (boost current, boost duration, WFR during wait phase or wait current) resulted in significant fluctuations in both voltage and current signals. This variation also influenced the thickness and morphology of the intermetallic layer at the interface. Since the growth of the intermetallic layer is primarily dependent on the level of heat input, this figure (Fig. 12) has been included to elucidate the relationship between intermetallic layer thickness and heat input as the characteristic parameters of the CMT process are altered.

The thickness presented in Fig. 12 is an average value, evaluated based on 25 measurements taken from 5 micrographs per sample, with five measurements taken in each micrograph at equal distances. Intermetallic layer thickness varies linearly with heat input for each parameter, except for some unusual variations attributed to the measurement strategy, since it was not possible to capture the thickness of spilled intermetallics when they were not attached to the intermetallic layer at some locations. Another possible cause for a decrease in thickness despite increasing heat input could be excessive wettability. Higher wettability, i.e., a higher contact area at the interface, facilitates faster dissipation of heat from the molten pool to the steel plate, which can also

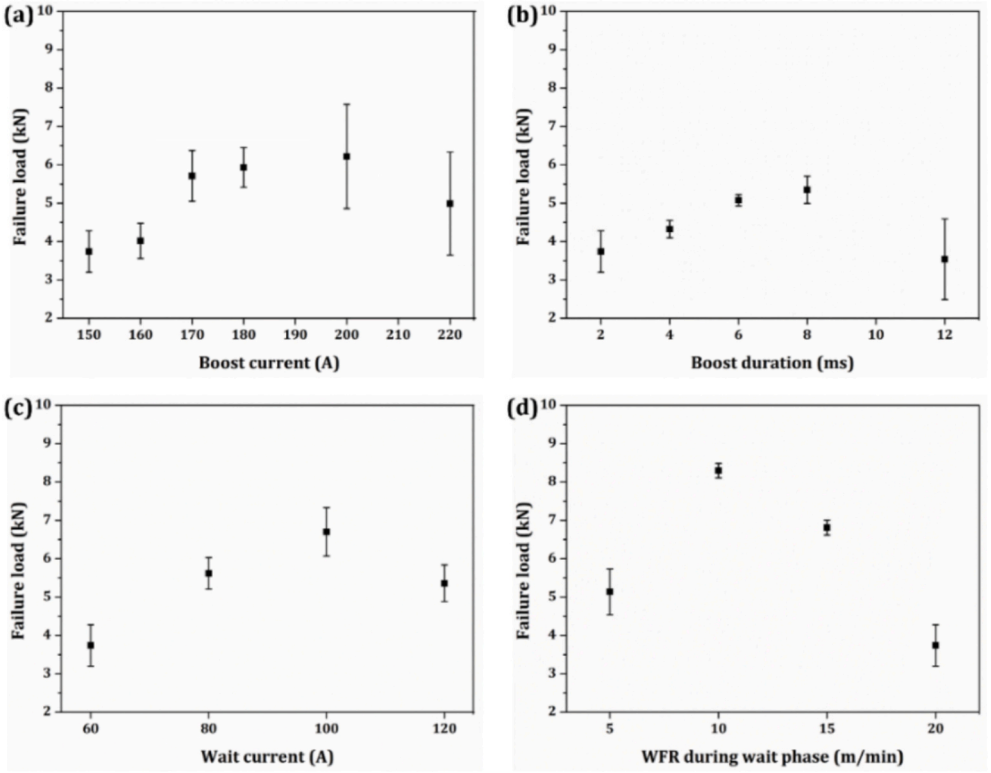

Fig. 13. Variation of failure load with different CMT characteristic parameters (a) boost current, (b) boost duration, (c) wait current, and (d) WFR during wait phase.

retard the growth of intermetallic phases. Thickness of the intermetallic layer was higher for boost duration and wait current parameters, with greater scatter compared to the other two parameters (boost current and WFR during the wait phase). The thickness was minimum for WFR during the wait phase and has a decreasing trend with increasing WFR during the wait phase, which can be attributed to the consumption of heat input for melting an increased volume of filler, thereby retarding the growth of intermetallic phases.

3.4. Shear-tensile testing

For overlap joints, calculating stress values is challenging due to ambiguity in defining the effective fracture area. Failure may occur at the interface, within the deposited bead, or in the base metal sheet, and accurately measuring the fractured area is often difficult. Additionally, overlap joints experience complex, non-uniform stress distributions across the bonded area due to factors such as shear stress concentration, bending, and peeling forces. This complexity means that a single stress value does not fully represent the joint's overall behaviour. In contrast, failure load provides a more straightforward and practical metric, as it directly reflects the joint's mechanical properties and does not rely on precise measurement of the fractured area. Considering the strong dependence of failure load on heat input and the corresponding growth of the intermetallic layer, shear-tensile tests were conducted to assess the integrity of the weld-brazed lap joints, with the results illustrated in Fig. 13. The failure load first increased in each case on increasing the boost current, boost duration and wait current and then decreased. This fall in the failure load can be attributed to both thicker intermetallic layer at the interface as well as excessive wettability of the joints at higher heat input levels. On the other hand, failure load decreased on increasing the WFR during the wait phase primarily due to reduction in wettability as well as weaker interfacial bonding. In this case, the thickness of the intermetallic layer also played an important role because the joins weld-brazed at 20 m/min WFR during the wait phase failed from the interface as the thickness of intermetallic layer was just 3.3 ± 0.4 μm. A maximum failure load of 8.3 ± 0.18 kN was observed at 10 m/min WFR during the wait phase and the thickness of intermetallic layer was 4.8 ± 1.1 μm. Out of all the samples tested, the second highest failure load was obtained at 200 A boost current and the intermetallic layer thickness was 4.78 ± 0.5 μm for this parameter. Thus, it can be inferred from these results that the samples with intermetallic layer thickness around 5 μm exhibit better mechanical strength. Too low intermetallic layer thickness leads to failure at premature loads due to weaker bonding whereas too thick intermetallic layer makes the interfacial region very brittle and prone to failure at comparatively lower loads. Yang et al. [3] reviewed the influence of intermetallic phases on Al/steel dissimilar joints and emphasized the importance of controlling the interfacial temperature and intermetallic layer thickness to achieve mechanically robust Al/steel joints.

Fig. 14 illustrates the locations and modes of failure for different joints during shear-tensile testing to better understand the cause of failure of joints. Four distinct failure modes were observed: at the interface (mode 1), along the fusion line (mode 2), within the bead (mode 3), and mixed mode failure (mode 4). These modes of failure were primarily influenced by the thickness of the intermetallic layer and the wettability of the joints. Joints with either insufficient wetting length or an excessively brittle interface failed at the interface. Fig. 14(a) shows the joint failure from the interface of sample 1 (as listed in Table 2). The primary cause of this failure was the insufficient interfacial contact area, which was inadequate to resist elongation under tensile load. Fig. 14(b) depicts the detached surfaces of this same joint. In contrast, Fig. 14(c) shows the joint failure of weld-brazed sample at a boost current of 170 A (sample 3 in Table 2). In this case, the failure was primarily due to the brittle nature of the interface. Fig. 14(d) displays the failure location of the joint weld-brazed at a wait current of 100 A. This joint failed along the boundary of the fusion zone, i.e., the fusion line (mode 2), and demonstrated a failure load of 6.7 ± 0.6 kN, the highest observed when varying the wait current. The joints failed in this mode when the interface was not excessively brittle and there was no humping in the bead. Fig. 14(e) shows the failure location of a joint weld-brazed at a

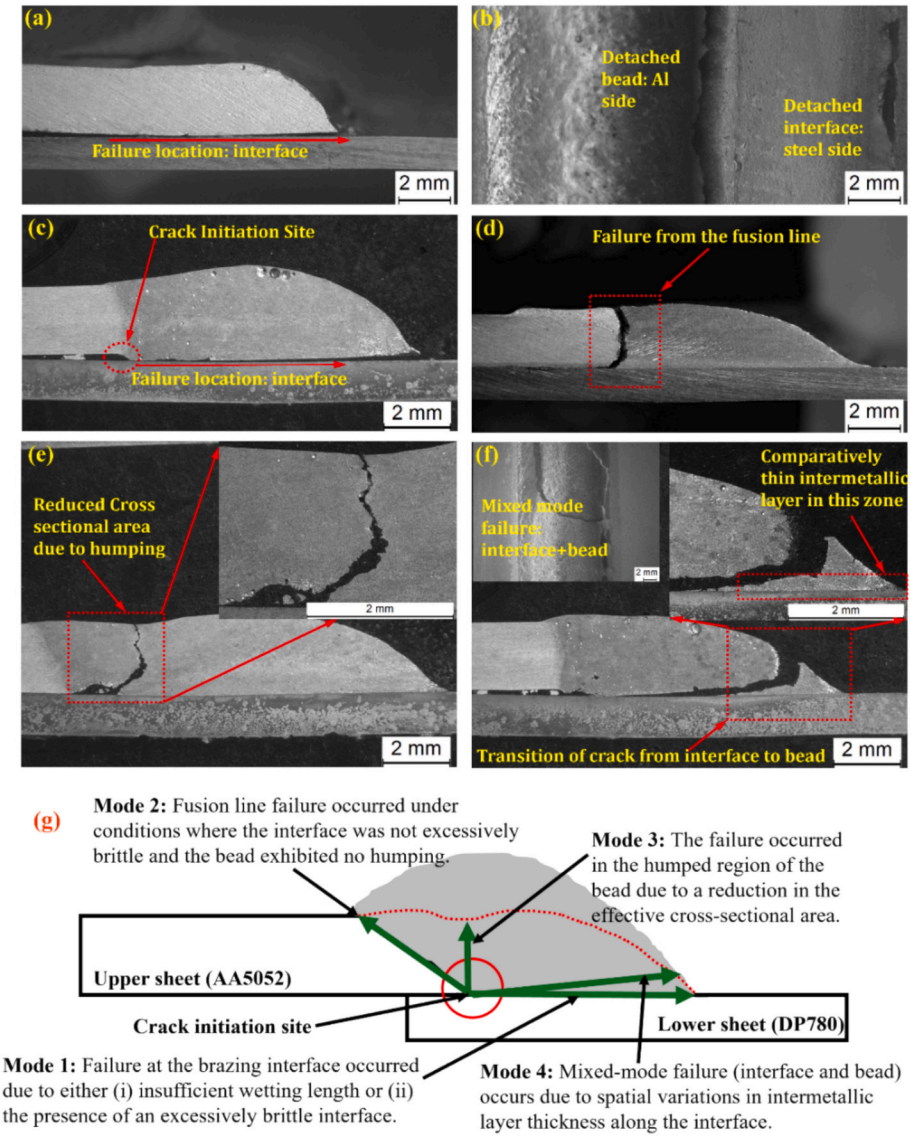

Fig. 14. Failure locations of weld-brazed joints: (a, b) lower interface (S1), (c) lower interface (S3), (d) fusion line (S12), (e) bead (S8), (f) mixed mode: interface + bead (S15), and (g) schematic of different failure modes.

boost duration of 6 ms. The failure occurred in the humped region of the bead (mode 3), where the occurrence of humping reduced the effective cross-sectional area. This humping resulted from the deposition of larger droplets as the boost duration increased.

Finally, Fig. 14(f) shows the failure location of the joint weld-brazed at a 10 m/min WFR during the wait phase. This joint corresponds to sample 15 in Table 2, which exhibited the highest failure load of 8.3 ± 0.18 kN among all the samples listed. The failure initiated at the interface and then the crack deviated into the bead (mode 4). This behaviour can be explained by the variation in intermetallic layer thickness at the interface. Typically, the intermetallic layer is thicker at the centre of the interface, and its thickness gradually decreases toward either the toe or root (refer to Fig. 11). Since the bead was strong enough to resist failure in this joint, the crack initiated at the root and propagated along the interface, which is brittle. The brittleness of the interface increases proportionally with the growth of the intermetallic layer. Lin et al. [47] reported that formation of intermetallic phases can reduce the ductility. In the present work, once the crack reached the thicker intermetallic layer zone, i.e., the centre of the interface, it deviated from the interface and propagated into the bead. Two factors contributed to the crack's propagation into the bead at this location: (i) the formation of a zinc-rich zone at the toe of the joint (refer to Fig. 11), and (ii) the extremely thin intermetallic layer near the toe. Thus, the joint failed in a mixed mode. In addition, Fig. 14(g) presents a schematic of all the failure modes along with the potential causes of each mode for better understanding. It is important to note that cracks initiated at the root in all the joints, as the gap between the sheets served as a crack initiation site and facilitated easy propagation from this point. Furthermore, the lap configuration joints experienced bending in addition to tensile loading due to the eccentricity between the sheet axes, which led to stress concentration at both the root and the toe of the deposited bead.

4. Conclusions

- The stability of the CMT weld-brazing is influenced by key parameters such as boost current, boost duration, wait current, and WFR. Analysis showed that process remains stable on increasing the boost current, while long boost durations or high wait currents can cause instability due to arc disturbances and premature filler deposition. Although the WFR affects deposition frequency, it has little impact on stability. Maintaining optimal boost duration and wait current is essential for stable CMT operation.

- Increasing the boost current, boost duration, and wait current enhances wettability, as evidenced by wider beads, longer wetting lengths, and smaller wetting angles. However, excessive wetting can lead to shrinkage and solidification cracking, particularly in steel-aluminium joints, due to rapid solidification and the brittle nature of the interface. Optimal control of these parameters is essential to balance wettability and avoid defects in the weld-brazed joints.
- The thickness of the intermetallic layer increased linearly with heat input, except in cases of excessive heat input or high wettability, which can reduce thickness. While boost current did not significantly alter the intermetallic layer thickness, higher boost durations and wait currents led to increased intermetallic growth and spilling into the fusion zone. Conversely, lower WFR's during the wait phase resulted in less pronounced spilling due to the deposition of larger droplets.
- Shear-tensile testing of weld-brazed lap joints revealed that the failure load increased with boost current, boost duration, and wait current up to an optimal point, after which it decreased. This decline in failure load was due to a thicker intermetallic layer and excessive wettability at higher heat inputs, or reduced wettability and weaker bonding at higher WFR's. Joints with an intermetallic layer thickness of around 5 μm demonstrated the highest mechanical strength, while both very thin and excessively thick layers led to lower failure loads.
- Failure modes varied with the intermetallic layer thickness and wettability, including interface, bead, and fusion line failures. The highest failure load was observed with a 10 m/min WFR, where failure originated at the interface and propagated into the bead, reflecting the complex interplay of intermetallic layer thickness and joint conditions.

CRediT authorship contribution statement

Jaivindra Singh: Writing – original draft, Methodology, Investigation, Formal analysis, Data curation, Conceptualization. **Kanwer Singh Arora:** Writing – review & editing, Validation, Supervision, Resources. **J.P. Oliveira:** Writing – review & editing, Writing – original draft, Supervision, Project administration, Funding acquisition.

Declaration of competing interest

The authors declare that they have no known competing financial interests or personal relationships that could have appeared to influence the work reported in this paper.

Acknowledgements

Jaivindra Singh and J.P. Oliveira acknowledge funding by national funds from FCT - Fundação para a Ciência e a Tecnologia, I.P., in the scope of the projects UIDP/50025/2020, LA/P/0037/2020, and UIDB/50025/2020 of the Associate Laboratory Institute of Nanostructures, Nanomodelling and Nanofabrication – i3N. The authors also acknowledge the support provided by the management and staff of Tata Steel Limited, Jamshedpur, India, throughout the course of this research, whenever and wherever it was needed.

References

[1] Pouranvari M, Abbasi M. Dissimilar gas tungsten arc weld-brazing of Al/steel using Al-Si filler metal: microstructure and strengthening mechanisms. J Alloys Compd 2018;749:121–7. https://doi.org/10.1016/j.jallcom.2018.03.224.
[2] Li Y, Wang H, Lai R, Yang B, Wang Z, Li Y. Effect of overlapping deposition strategy on microstructure and mechanical properties of Al-clad steel by AFSD. J Manuf Process 2024;129:51–61. https://doi.org/10.1016/j.jmapro.2024.08.044.
[3] Yang Y, Luo Z, Zhang Y, Su J. Dissimilar welding of aluminium to steel: a review. J Manuf Process 2024;110:376–97. https://doi.org/10.1016/j.jmapro.2023.12.060.
[4] Asati B, Kishore K, Shajan N, Arora KS. Investigation of a novel stepped-current vis-à-vis conventional resistance spot welding of dual-phase 780 (DP 780) steel. J Manuf Process 2024;126:382–401. https://doi.org/10.1016/j.jmapro.2024.07.077.
[5] Shiran MKG, Khalaj G, Pouraliakbar H, Jandaghi MR, Dehnavi AS, Bakhtiari H. Multilayer Cu/Al/Cu explosive welded joints: characterizing heat treatment effect on the interface microstructure and mechanical properties. J Manuf Process 2018;35:657–63. https://doi.org/10.1016/j.jmapro.2018.09.014.
[6] Bin Mamat S, Tashiro S, Masri MN, Hong SM, Bang HS, Tanaka M. Application of pulse plasma MIG welding process to Al/steel dissimilar joining. Welding in the World 2020;64:857–71. https://doi.org/10.1007/s40194-020-00879-2.
[7] Pouraliakbar H, Khalaj G, Jandaghi MR, Fadaei A, Ghareh-Shiran MK, Shim SH, et al. Three-layered SS321/AA1050/AA5083 explosive welds: effect of PWHT on the interface evolution and its mechanical strength. Int J Pressure Vessels Piping 2020:188. https://doi.org/10.1016/j.ijpvp.2020.104216.
[8] Singh J, Singh A, Arora KS, Shukla DK. Multi-objective optimization of process parameters during dissimilar cold metal transfer weld-brazing of Al-steel. Transactions of the Indian Institute of Metals 2022;75:1929–40. https://doi.org/10.1007/s12666-022-02567-9.
[9] Wang H, Han R, Zhang Z, Zhu M, Liu L. Riveting–welding hybrid bonding of high-strength steel and aluminum alloy. Materials and Manufacturing Processes 2019;34:1671–80. https://doi.org/10.1080/10426914.2019.1683574.
[10] Beygi R, Galvão I, Akhavan-Safar A, Pouraliakbar H, Fallah V, da Silva LFM. Effect of alloying elements on intermetallic formation during friction stir welding of dissimilar metals: a critical review on aluminum/steel. Metals (Basel) 2023:13. https://doi.org/10.3390/met13040768.
[11] Ma H, Qin G, Geng P, Ao Z, Chen Y. Effect of intermetallic compounds on the mechanical property and corrosion behaviour of aluminium alloy/steel hybrid fusion-brazed welded structure. J Manuf Process 2022;75:170–80. https://doi.org/10.1016/j.jmapro.2022.01.004.
[12] Song JL, Lin SB, Yang CL, Fan CL, Ma GC. Analysis of intermetallic layer in dissimilar TIG welding-brazing butt joint of aluminium alloy to stainless steel. Science and Technology of Welding and Joining 2010;15:213–8. https://doi.org/10.1179/136217110X12665048207610.
[13] Basak S, Das H, Pal TK, Shome M. Characterization of intermetallics in aluminum to zinc coated interstitial free steel joining by pulsed MIG brazing for automotive application. Mater Charact 2016;112:229–37. https://doi.org/10.1016/j.matchar.2015.12.030.
[14] Mohammadpour M, Yazdian N, Wang HP, Carlson B, Kovacevic R. Effect of filler wire composition on performance of Al/Galvanized steel joints by twin spot laser welding-brazing method. J Manuf Process 2018;31:20–34. https://doi.org/10.1016/j.jmapro.2017.11.007.
[15] Singh J, Kanwer, Arora S, Shajan N, Shome M, Dinesh, et al. Influence of wire feed rate to speed ratio on arc stability and characteristics of cold metal transfer weld-brazed dissimilar joints. The International Journal of Advanced Manufacturing Technology 2020;108:3491–505. https://doi.org/10.1007/s00170-020-05637-8/Published.
[16] Dai G, Liu Y, Chen K, Liu W, Wang T, Huang Q. Effect of cumulative deformation and interlayer mechanical properties on bonding strength of corrugated interface steel/aluminum composite plate. J Manuf Process 2023;103:78–89. https://doi.org/10.1016/j.jmapro.2023.08.028.
[17] Wu H, Yang G, Li Y, Lei M, Li X, Li Y. Investigating the influence of Ni interlayers on Fe/Al laser welded joints: a first-principles study. J Mater Res Technol 2024;30:7485–94. https://doi.org/10.1016/j.jmrt.2024.05.032.
[18] Singh J, Arora KS, Shukla DK. Lap weld-brazing of aluminium to steel using novel cold metal transfer process. J Mater Process Technol 2020:283. https://doi.org/10.1016/j.jmatprotec.2020.116728.
[19] Zhang C, Wu M, Pu J, Shan Q, Sun Y, Wang S, et al. Effect of Cu coating on microstructure and properties of Al/steel welding–brazing joints obtained by cold metal transfer (CMT). Coatings 2022:12. https://doi.org/10.3390/coatings12081123.
[20] Niu S, Chen S, Dong H, Zhao D, Zhang X, Guo X, et al. Microstructure and properties of lap joint between aluminum alloy and galvanized steel by CMT. J Mater Eng Perform 2016;25:1839–47. https://doi.org/10.1007/s11665-016-2035-2.
[21] Song JL, Lin SB, Yang CL, Fan CL. Effects of Si additions on intermetallic compound layer of aluminum-steel TIG welding-brazing joint. J Alloys Compd 2009;488:217–22. https://doi.org/10.1016/j.jallcom.2009.08.084.
[22] Pouranvari M. Critical assessment: dissimilar resistance spot welding of aluminium/steel: challenges and opportunities. Materials Science and Technology (United Kingdom) 2017;33:1705–12. https://doi.org/10.1080/02670836.2017.1334310.
[23] Milani AM, Paidar M, Khodabandeh A, Nategh S. Influence of filler wire and wire feed speed on metallurgical and mechanical properties of MIG welding–brazing of automotive galvanized steel/5754 aluminum alloy in a lap joint configuration. Int J Adv Manuf Technol 2016;82:1495–506. https://doi.org/10.1007/s00170-015-7505-4.
[24] Niu S, Chen S, Dong H, Zhao D, Zhang X, Guo X, et al. Microstructure and properties of lap joint between aluminum alloy and galvanized steel by CMT. J Mater Eng Perform 2016;25:1839–47. https://doi.org/10.1007/s11665-016-2035-2.
[25] Singh J, Arora KS, Shukla DK, Kumar H. Mechanical and microstructural characterization of cold metal transfer (CMT) spot aluminium-steel weld-brazed joints. Proceedings of the Institution of Mechanical Engineers, Part L: Journal of Materials: Design and Applications 2022;236:2506–15. https://doi.org/10.1177/14644207221097709.

[26] Xie B, Xue J, Ren X, Wu W, Lin Z. A comparative study of the CMT+P process on 316L stainless steel additive manufacturing. Applied Sciences (Switzerland) 2020: 10. https://doi.org/10.3390/app10093284.
[27] Mou G, Hua X, Wu D, Zhang Y, Wang D, Chu W. Study on weld seam surface deposits of CuSi3 CMT brazing. Int J Adv Manuf Technol 2017;92:2735–42. https://doi.org/10.1007/s00170-017-0349-3.
[28] Pang J, Hu S, Shen J, Wang P, Liang Y. Arc characteristics and metal transfer behavior of CMT + P welding process. J Mater Process Technol 2016;238:212–7. https://doi.org/10.1016/j.jmatprotec.2016.07.033.
[29] Zhang Z, Li H, He S, Zhou W, Qi Y. Improving forming quality and corrosion resistance of CMT-P additive manufactured 2024 aluminum alloy using assisted laser. J Manuf Process 2024;124:1025–36. https://doi.org/10.1016/j.jmapro.2024.06.071.
[30] Chen M, Zhang D, Wu C. Current waveform effects on CMT welding of mild steel. J Mater Process Technol 2017;243:395–404. https://doi.org/10.1016/j.jmatprotec.2017.01.004.
[31] Zhou S, Xie H, Ni J, Yang G, Qin L, Guo X. Metal transfer behavior during CMT-based wire arc additive manufacturing of Ti-6Al-4V alloy. J Manuf Process 2022; 82:159–73. https://doi.org/10.1016/j.jmapro.2022.07.063.
[32] Hu Y, Chen F, Cao S, Fan Y, Xie R. Preparation and characterization of CMT wire arc additive manufacturing Al-5%Mg alloy depositions through assisted longitudinal magnetic field. J Manuf Process 2023;101:576–88. https://doi.org/10.1016/j.jmapro.2023.05.104.
[33] Zhang Z, Shen J, Hu S, Chen Y, Yin C, Bu X. Optimization of CMT characteristic parameters for swing arc additive manufacturing of AZ91 magnesium alloy based on process stability analysis. Materials 2023;16. https://doi.org/10.3390/ma16083236.
[34] Karimi MR, Wang SH, Jelovica J. Taguchi-based experimental investigation into weld cladding of Ni-WC MMC overlays by CMT process. Int J Adv Manuf Technol 2022;122:2433–61. https://doi.org/10.1007/s00170-022-09816-7.
[35] Chen M, Zhang D, Wu C. Current waveform effects on CMT welding of mild steel. J Mater Process Technol 2017;243:395–404. https://doi.org/10.1016/j.jmatprotec.2017.01.004.
[36] Zhao Y, Chen F, Cao S, Chen C, Xie R. Effect of CMT welding heat input on microstructure and properties of 2A14 aluminum alloy joint. Metals (Basel) 2022: 12. https://doi.org/10.3390/met12122100.
[37] Pepe N, Egerland S, Colegrove PA, Yapp D, Leonhartsberger A, Scotti A. Measuring the process efficiency of controlled gas metal arc welding processes. Science and Technology of Welding and Joining 2011;16:412–7. https://doi.org/10.1179/1362171810Y.0000000029.
[38] Yu J, Kim D. Effects of welding current and torch position parameters on minimizing the weld porosity of zinc-coated steel. Int J Adv Manuf Technol 2018; 95:551–67. https://doi.org/10.1007/s00170-017-1180-6.
[39] Singh J, Singh Arora K, Kumar Shukla D. High cycle fatigue performance of cold metal transfer (CMT) brazed C-Mn-440 steel joints. Int J Fatigue 2020:137. https://doi.org/10.1016/j.ijfatigue.2020.105663.
[40] Zhang HT, Feng JC, He P, Zhang BB, Chen JM, Wang L. The arc characteristics and metal transfer behaviour of cold metal transfer and its use in joining aluminium to zinc-coated steel. Mater Sci Eng A 2009;499:111–3. https://doi.org/10.1016/j.msea.2007.11.124.
[41] Padma Rao A, Hadi M, Rajendran C, Tushar S, Ivanov M, Senthil Kumar P, et al. Potentiodynamic corrosion behavior and microstructural characteristics of pulsed CMT-welded AA2014-T6 aluminium alloy joints: effect of PWHT. Advances in Materials Science and Engineering 2022;2022. https://doi.org/10.1155/2022/4874834.
[42] Pickin CG, Williams SW, Lunt M. Characterisation of the cold metal transfer (CMT) process and its application for low dilution cladding. J Mater Process Technol 2011;211:496–502. https://doi.org/10.1016/j.jmatprotec.2010.11.005.
[43] Gomez Ortega A, Corona Galvan L, Deschaux-Beaume F, Mezrag B, Rouquette S. Effect of process parameters on the quality of aluminium alloy Al5Si deposits in wire and arc additive manufacturing using a cold metal transfer process. Science and Technology of Welding and Joining 2018;23:316–32. https://doi.org/10.1080/13621718.2017.1388995.
[44] Ortega AG, Galvan LC, Rouquette S, Deschaux-Beaume F, Ortega AG, Galvan LC, et al. Effect of welding parameters on the quality of multilayer deposition of aluminum alloy. In: Advances in materials & processing technologies conference. Vellore: HAL Open Science; 2017.
[45] Singh J, Arora KS, Shukla DK. Dissimilar MIG-CMT weld-brazing of aluminium to steel: a review. J Alloys Compd 2019;783:753–64. https://doi.org/10.1016/j.jallcom.2018.12.336.
[46] Xia H, Yang B, Han Y, Xu L, Tan C, Li L, et al. Toward understanding the fractured mechanism in laser welded–brazed Al/steel interface by in–situ SEM tensile observations. J Mater Process Technol 2024:325. https://doi.org/10.1016/j.jmatprotec.2024.118294.
[47] Lin D, Hu J, Wu R, Liu Y, Li X, SaGong MJ, et al. Multiscale plastic deformation in additively manufactured FeCoCrNiMox high-entropy alloys to achieve strength–ductility synergy at elevated temperatures. Int J Plast 2024:183. https://doi.org/10.1016/j.ijplas.2024.104142.